Role of inertia in nonequilibrium steady states of sheared binary fluids

Suzanne M. Fielding*
School of Mathematics and Manchester Centre for Nonlinear Dynamics, University of Manchester, Oxford Road, Manchester M13 9PL, United Kingdom
(Received 16 October 2007; published 21 February 2008)

We study numerically phase separation in a binary fluid subject to an applied shear flow in two dimensions, with full hydrodynamics. To do so, we introduce a mixed finite-differencing and spectral simulation technique, with a transformation to render trivial the implementation of Lees-Edwards sheared periodic boundary conditions. For systems with inertia, we reproduce the nonequilibrium steady states reported in a recent lattice Boltzmann study. The domain coarsening that would occur in zero shear is arrested by the applied shear flow, which restores a finite-domain-size set by the inverse shear rate. For inertialess systems, in contrast, we find no evidence of nonequilibrium steady states free of finite-size effects: Coarsening persists indefinitely until the typical domain size attains the system size, as in zero shear. We present an analytical argument that supports this observation and that furthermore provides a possible explanation for a hitherto puzzling property of the nonequilibrium steady states with inertia.

DOI: 10.1103/PhysRevE.77.021504 PACS number(s): 64.75.−g, 47.11.Qr

I. INTRODUCTION

When an initially homogeneous mixture of two incompressible fluids (A and B) undergoes a deep temperature quench into the spinodal regime, it becomes unstable with respect to spatial fluctuations in the composition field $\phi(\boldsymbol{x},t)$. The mixture then phase separates into well-defined domains of A-rich and B-rich fluids, which, after a rapid initial transient, attain local equilibrium within each domain. The system remains globally out of equilibrium on long time scales, however, due to the excess energy that resides in the interfaces between the domains. Here we consider the maximally symmetric case of a 50:50 mixture of two mutually phobic fluids with matched viscosities and densities.

Following the initial transient of their formation, the domains slowly coarsen in time through the action of the surface tension in the interfaces that separate them. (For reviews of phase-ordering kinetics, see Refs. [1–3].) In this way, the excess interfacial energy of the system progressively relaxes towards its minimal equilibrium value. This coarsening process proceeds through three distinct regimes that are successively dominated by diffusive, viscous, and inertial dynamics. In the limit of an infinite system size $\Lambda\to\infty$ (taken first), the typical domain size perpetually increases without bound: the system never globally equilibrates, even in the limit of infinite time $t\to\infty$ (taken second). For any finite system size, coarsening is in practice eventually cut off once the typical domain size $L(t)$ attains the system size Λ.

Besides these systems that remain out of equilibrium as they slowly relax towards a fully phase-separated state, another class of systems comprises those that are continuously driven out of equilibrium by the external application of a steady shear flow. In this paper, we consider systems that are *both* undergoing phase separation *and* simultaneously subject to an applied shear flow. They thus combine both of the nonequilbrium features just described. The main question that we address is whether shear interrupts domain coarsening and restores a nonequilibrium steady state with a typical domain size $L(\dot{\gamma}^{-1})$ set by the inverse of the applied shear rate $\dot{\gamma}$ or whether coarsening persists indefinitely, up to the system size, as in zero shear.

Despite previous experimental [4–14], numerical [15–31], and theoretical [18–21,29,32–37] work, this question remained open until the recent simulation studies of Stansell and co-workers [38,39]. Using lattice Boltzmann techniques, they gave convincing evidence for the formation of nonequilibrium steady states, with domains of a finite size set by the inverse shear rate, independent of the system size. The domain morphology inherits the anisotropy of the applied shear flow and is therefore characterized by two length scales $L_{\parallel}$ and $L_{\perp}$, respectively describing the major and minor domain axes. A remarkable achievement of Refs. [38,39] was the exploration, by judicious parameter steering, of a range of inverse shear rates spanning six decades on a scaling plot. For reasons discussed below this range would, *a priori*, be expected to encompass two different regimes, separately dominated by viscous and inertial dynamics. Surprising, therefore, is the observation of an apparently single scaling with shear rate for each of $L_{\parallel}$ and $L_{\perp}$, across all six decades.

All the simulations reported in Refs. [38,39] have nonzero fluid inertia. Indeed, even when attempting to access the limit of zero inertia, a small but nonzero inertia remains a practical requirement of the lattice Boltzmann technique. In this paper, we investigate phase separation under shear in systems that are strictly inertialess. To do so, we apply a different simulation technique to this problem, comprising finite differencing combined with Fourier spectral methods. We also use a convenient transformation to render trivial the implementation of sheared periodic boundary conditions [40].

Our main numerical result will be that, in truly inertialess systems, coarsening persists indefinitely, up to the system size, despite the external shear flow. We will also present an analytical argument that supports this observation. A simple extension to the same argument provides a possible explanation for the existence of a single scaling for each of $L_{\parallel}$ and $L_{\perp}$ across all six decades of scaled shear rate in the simulations of Ref. [38], with inertia.

*suzanne.fielding@manchester.ac.uk

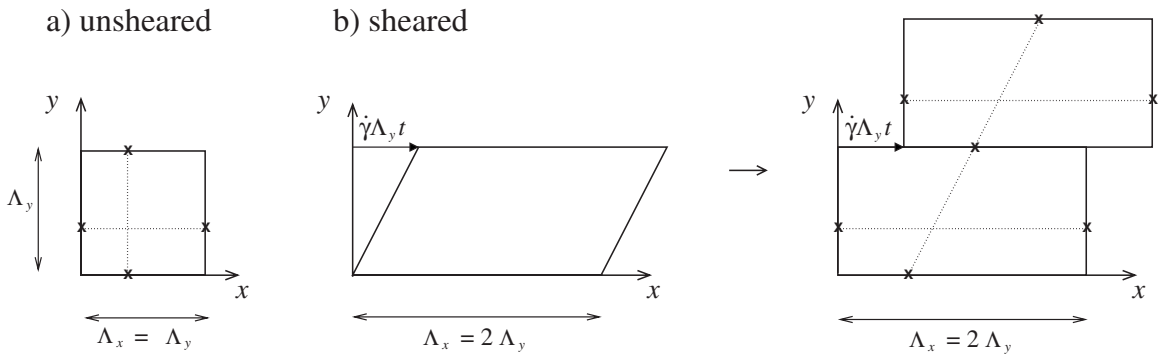

FIG. 1. Flow geometries in the (a) unsheared and (b) sheared cases. The crossed connected by thin dotted lines show representative pairs of points connected by periodic boundary conditions.

We start by introducing the model equations, flow geometry, and choice of units in Secs. II–IV, respectively. In Sec. V we briefly outline our numerical method, of which further details are given in the Appendixes. The length and time scales that characterize demixing are presented in Sec. VI, leading to a discussion in Sec. VII of the choice of parameter values in our simulations. In Sec. VIII we present our numerical results, starting in Sec. VIII A with the case of coarsening in zero shear, before considering an applied shear flow with and without inertia in Secs. VIII B and VIII D, respectively. Section VIII C contains a linking discussion. Our aim in Secs. VIII A and VIII B is simply to reproduce the behavior seen in previous lattice Boltzmann studies [38,41,42], thereby gaining confidence in our own simulation method. In Sec. IX we present an analytical argument that supports our numerical observations, as well as those of Ref. [38]. Section X contains a summary and an outlook to future work.

II. GOVERNING EQUATIONS

The fluid velocity field $\boldsymbol{v}(\boldsymbol{x},t)$ and pressure $p(\boldsymbol{x},t)$ are governed by the Navier-Stokes equation

$$\rho(\partial_t \boldsymbol{v} + \boldsymbol{v}\cdot\boldsymbol{\nabla}\boldsymbol{v}) = \eta\nabla^2\boldsymbol{v} - \phi\boldsymbol{\nabla}\mu - \boldsymbol{\nabla}p \tag{1}$$

together with the incompressibility constraint

$$\boldsymbol{\nabla}\cdot\boldsymbol{v} = 0. \tag{2}$$

Here ρ is the fluid density and η the viscosity. $p(\boldsymbol{x},t)$ is the thermodynamic part of the pressure tensor and $\mu(\boldsymbol{x},t)$ is a chemical potential, defined below. In what follows, we shall consider two-dimensional (2D) flow in the x-y plane with velocity components v_x and v_y.

To eliminate the pressure, we take the curl of Eq. (1). The z component of the resulting equation is

$$\rho(\partial_t \omega + \boldsymbol{v}\cdot\boldsymbol{\nabla}\omega) = \eta\nabla^2\omega - [\boldsymbol{\nabla}\wedge\phi\boldsymbol{\nabla}\mu]\cdot\hat{\boldsymbol{z}}, \tag{3}$$

in which the vorticity ω obeys

$$\boldsymbol{\nabla}\wedge\boldsymbol{v} = \omega\hat{\boldsymbol{z}}. \tag{4}$$

To ensure that the incompressibility constraint (2) is automatically obeyed, we define a stream function ψ via

$$\boldsymbol{v} = \boldsymbol{\nabla}\wedge\psi\hat{\boldsymbol{z}}, \tag{5}$$

which is related to the vorticity as follows:

$$\omega = -\nabla^2\psi. \tag{6}$$

The dynamics of the compositional order parameter $\phi(\boldsymbol{x},t)$ is prescribed by an advection-diffusion equation of Cahn-Hilliard type (see Refs. [2,43]):

$$\partial_t\phi + \boldsymbol{v}\cdot\boldsymbol{\nabla}\phi = M\nabla^2\mu. \tag{7}$$

Here M is the mobility, assumed constant, controlling the rate of intermolecular diffusion. The chemical potential

$$\mu = G\phi(\phi^2 - 1) - \kappa\nabla^2\phi, \tag{8}$$

in which G is a positive constant with the dimensions of stress. κ is also a positive constant, controlling the characteristic width l of the interface between domains:

$$l = \left(\frac{\kappa}{G}\right)^{1/2}. \tag{9}$$

The surface tension of the interface is given by

$$\sigma = \frac{2\sqrt{2}lG}{3}. \tag{10}$$

III. FLOW GEOMETRY

In the absence of shear we consider a square domain of size $\Lambda_x = \Lambda_y$ in the x-y plane [Fig. 1(a)]. We adopt periodic boundary conditions in each direction:

$$\phi(x=0,y) = \phi(x=\Lambda_x,y) \quad \forall \quad y, \tag{11}$$

$$\phi(x,y=0) = \phi(x,y=\Lambda_y) \quad \forall \quad x, \tag{12}$$

and similarly for v_x, v_y, ψ, and ω.

To study shear, we consider a system that is rectangular with $\Lambda_x=2\Lambda_y$. Conceptually, a shear flow of rate $\dot{\gamma}$ is applied by moving the upper boundary to the right at a constant speed $\dot{\gamma}\Lambda_y$, as shown in Fig. 1(b) (left), so that the velocity field then has a constant affine part $\dot{\gamma}y\hat{\boldsymbol{x}}$ and an additive fluctuating contribution $\tilde{\boldsymbol{v}}(\boldsymbol{x},t)$. In practice, this is implemented via Lees-Edwards sliding periodic boundary conditions [Fig. 1(b), right], such that the system has no physical borders but instead comprises an infinitely repeating array of images arranged in horizontally sliding layers. The boundary conditions are then

$$\phi(x=0,y)=\phi(x=\Lambda_x,y) \quad \forall \quad y, \tag{13}$$

$$\phi(x,y=0)=\phi(x+\dot{\gamma}\Lambda_y t,y=\Lambda_y) \quad \forall \quad x. \tag{14}$$

These also apply to $\tilde{v}_x$ and $\tilde{v}_y$, as well as the corresponding fluctuating contribution to the stream function $\tilde{\psi}$ and vorticity $\tilde{\omega}$.

IV. CHOICE OF UNITS

The model equations contain five parameters ρ, η, M, G, and l. (We must specify two of G, l, κ, and σ, and here have chosen G and l.) In addition, we must also specify the system's dimensions Λ_x and Λ_y and the applied shear rate $\dot{\gamma}$, making eight parameters in all. Three of these can be eliminated by choosing appropriate units for length, time, and stress. Accordingly, we measure lengths in units of the vertical system size $\Lambda_y\equiv 1$, stresses in units of $G\equiv 1$, and times in units of the characteristic "microscopic" time for diffusion across an interface,

$$\tau_0=\frac{(\sqrt{2}l)^3}{3M\sigma}\equiv 1. \tag{15}$$

In these units, the governing equations comprise Eqs. (3), (5), and (6) (unchanged) together with

$$\partial_t\phi+\boldsymbol{v}\cdot\boldsymbol{\nabla}\phi=l^2\nabla^2\mu \tag{16}$$

and

$$\mu=\phi(\phi^2-1)-l^2\nabla^2\phi. \tag{17}$$

This leaves the rescaled density ρ, viscosity η, interfacial width l, aspect ratio Λ_x, and applied shear rate $\dot{\gamma}$ as the five control parameters. In our numerical work we fix Λ_x and l, varying ρ, η, and $\dot{\gamma}$ between runs.

V. NUMERICAL METHOD

In the laboratory frame, the numerical implementation of sheared periodic boundary conditions is rather involved. We now discuss a convenient transformation that renders it trivial [40]. We do so here in outline only, referring the interested reader to Appendix A for details.

The transformation comprises two steps. In the first, the velocity field is expressed as the sum of a constant affine part and a fluctuating contribution:

$$\boldsymbol{v}(\boldsymbol{x},t)=\dot{\gamma}y\hat{\boldsymbol{x}}+\tilde{\boldsymbol{v}}(\boldsymbol{x},t). \tag{18}$$

In the second step, we transform to the cosheared frame

$$(x,y,t)\rightarrow(x'=x-\dot{\gamma}ty,y'=y,t'=t), \tag{19}$$

defining for convenience the cosheared gradient operator

$$\boldsymbol{\nabla}_c=\hat{\boldsymbol{x}}\partial_{x'}+\hat{\boldsymbol{y}}(-\dot{\gamma}t\partial_{x'}+\partial_{y'}). \tag{20}$$

As shown in Appendix A, the final transformed equation set, dropping the primes for clarity, is then

$$\omega=-\nabla_c^2\psi, \tag{21}$$

together with

$$\rho\partial_t\omega+\rho(\partial_y\psi\partial_x\omega-\partial_x\psi\partial_y\omega)=\eta\nabla_c^2\omega-[\partial_x\phi\partial_y\mu-\partial_y\phi\partial_x\mu], \tag{22}$$

$$\partial_t\phi+(\partial_y\psi\partial_x\phi-\partial_x\psi\partial_y\phi)=l^2\nabla_c^2\mu, \tag{23}$$

$$\mu=\phi(\phi^2-1)-l^2\nabla_c^2\phi. \tag{24}$$

A priori, the bracketed expressions in Eqs. (22) and (23) contain terms in the applied shear rate $\dot{\gamma}$. However, in each bracket these are equal and opposite, and so cancel. An equivalent statement is that the bracketed expressions are invariant under shear.

This transformation considerably simplifies the implementation of an applied shear flow. Indeed, looking at Eqs. (21)–(24) we see that the only effect of shear is to renormalize the gradient operator $\boldsymbol{\nabla}\rightarrow\boldsymbol{\nabla}_c$. Furthermore, the dynamical variables ϕ, ψ, and ω are now subject to *ordinary* periodic boundary conditions:

$$\phi(x=0,y)=\phi(x=\Lambda_x,y) \quad \forall \quad y,$$

$$\phi(x,y=0)=\phi(x,y=\Lambda_y) \quad \forall \quad x, \tag{25}$$

and similarly for ψ and ω. This will allow us to use Fourier transforms in our numerical algorithm, as described below.

Under the transformation described so far, the relative shear of the laboratory and cosheared frames becomes large at long times, diverging at a constant rate $\dot{\gamma}$. This is clearly expected to give rise to numerical instabilities. To circumvent this problem, once the relative shear $s(t)$ attains $\Lambda_x/2\Lambda_y$ we perform by hand an instantaneous shift $s(t)\rightarrow s(t)-\Lambda_x/\Lambda_y$. In this way, the function $s(t)$ is bounded between $s=-\Lambda_x/2\Lambda_y$ and $s=\Lambda_x/2\Lambda_y$, comprising a sawtooth with sections of constant slope $\dot{\gamma}$ connected by negative step discontinuities of height Λ_x/Λ_y at equal time intervals $\Delta t=\Lambda_x/\dot{\gamma}\Lambda_y$. Because this shift involves moving the upper wall by exactly one multiple of the system length, the periodic boundary conditions (25) are unaffected. For times between these shifts, the sole effect of this modification appears

in the cosheared gradient operator, which, in place of Eq. (20), is now

$$\nabla_c = \hat{\mathbf{x}}\partial_x + \hat{\mathbf{y}}[-s(t)\partial_x + \partial_y]. \tag{26}$$

The special case of zero shear is trivially achieved by setting $s(t)=0\ \forall t$.

In Appendix B, we discuss the numerical algorithm used to study the dynamical evolution of $\phi(\boldsymbol{x},t)$, $\omega(\boldsymbol{x},t)$, and $\psi(\boldsymbol{x},t)$, as specified by Eqs. (21)–(24) and (26). Readers who are not interested in these issues can skip straight to Sec. VI without losing any of the argument.

VI. LENGTH SCALES AND TIME SCALES

Following a deep temperature quench of an unsheared system into the two-phase regime, well-defined domains of each phase form, separated by sharp interfaces. See Fig. 3, for example, in which the white (black) patches are domains of A- (B-) rich fluid. After a nonuniversal transient associated with their initial formation, these domains progressively grow in size through the action of surface tension, passing through regimes that are successively dominated by diffusive, viscous, and inertial dynamics. During this process of domain coarsening, the dynamical scaling hypothesis [2,44,45] states that any structural length scale $L(t)$ characterizing the typical domain size (e.g., as measured by some moment of the structure factor) should depend in the same way on time t as any other (e.g., as measured by the total amount of interface present in the system). Within each regime, dimensional analysis can be used to construct the functional form of $L(t)$ out of the model parameters that are relevant to that regime [44,45].

In the diffusive regime, the system is unaware of the density ρ and the viscosity η. Out of the remaining parameters M, σ, and the time t we can construct only one length scale

$$L_{\mathrm{D}}(t) = (M\sigma t)^{1/3}. \tag{27}$$

In our units $L_{\mathrm{D}}=\alpha l t^{1/3}$ with $\alpha=(2\sqrt{2}/3)^{1/3}$.

In the viscous hydrodynamic regime, the system is unaware of M and ρ. From the remaining parameters η, σ, and t we have

$$L_{\mathrm{V}}(t) = \frac{\sigma t}{\eta}. \tag{28}$$

In our units $L_{\mathrm{V}}=\alpha^3 l t/\eta$.

In the inertial hydrodynamic regime, the system is unaware of M and η. From the remaining parameters ρ, σ, and t we have

$$L_{\mathrm{I}}(t) = \left(\frac{\sigma t^2}{\rho}\right)^{1/3}. \tag{29}$$

In our units $L_{\mathrm{I}}=\alpha(l t^2/\rho)^{1/3}$.

By equating the growth laws $L_{\mathrm{D}}=L_{\mathrm{V}}$, we can construct the characteristic length scale L_{DV} at which we expect a crossover from diffusive to viscous dynamics. Similarly by equating $L_{\mathrm{V}}=L_{\mathrm{I}}$ we find the length scale L_{VI} for crossover from viscous to inertial dynamics. Together with the "microscopic" interfacial width l and the system size Λ_x,Λ_y, we then have the following basic length scales.

(i) The interfacial width l.

(ii) The characteristic length scale for crossover from diffusive to viscous hydrodynamic coarsening:

$$L_{\mathrm{DV}} = \sqrt{M\eta}. \tag{30}$$

In our units $L_{\mathrm{DV}}=l\sqrt{\eta}$.

(iii) The characteristic length scale for crossover from viscous to inertial hydrodynamic coarsening:

$$L_{\mathrm{VI}} = \frac{\eta^2}{\rho\sigma}. \tag{31}$$

In our units $L_{\mathrm{VI}}=3\eta^2/2\sqrt{2}\rho l$.

(iv) The system size Λ_x,Λ_y. In our units $\Lambda_y=1$ always.

Corresponding to these are the following time scales.

(i) The microscopic time scale for diffusion across an interface:

$$\tau_0 = \frac{2\sqrt{2}}{3}\frac{l^3}{M\sigma} = 1. \tag{32}$$

(ii) The characteristic time scale for crossover from diffusive to viscous hydrodynamic coarsening:

$$T_{\mathrm{DV}} = \frac{\sqrt{M\eta^3}}{\sigma} = \frac{3}{2\sqrt{2}}\eta^{3/2}. \tag{33}$$

(iii) The characteristic time scale for crossover from viscous to inertial hydrodynamic coarsening:

$$T_{\mathrm{VI}} = \frac{\eta^3}{\rho\sigma^2} = \frac{9}{8}\frac{\eta^3}{\rho l^2}. \tag{34}$$

(iv) The characteristic time at which the domain size attains the system size in coarsening:

$$T_{\mathrm{system}}. \tag{35}$$

So far we have discussed the growing structural length scale $L(t)$ in general terms, without any specific definition. In fact, there exist many possible measures of the characteristic domain size. In zero shear we use the following one:

$$L_s = \left(\frac{\int dq_x \int dq_y S(\boldsymbol{q})}{\int dq_x \int dq_y |q|^{-1} S(\boldsymbol{q})}\right)^{-1}, \tag{36}$$

defined via the structure factor $S(\boldsymbol{q})$, which, as usual, is the 2D Fourier transform of $\phi(x,y)$.

The discussion so far in this section has related to unsheared systems. Under an applied shear flow the domain

morphology becomes anisotropic. See Fig. 6, for example. Accordingly, we consider the matrix [28,38]

$$D_{\alpha\beta} = \frac{l \int dx \int dy \partial_\alpha \phi \partial_\beta \phi}{\int dx \int dy \phi^2}, \tag{37}$$

the reciprocal eigenvalues of which give us two length scales $L_\parallel$ and $L_\perp$ characterizing the long and short principal axes of the domain morphology.

VII. PARAMETER STEERING

As discussed in Sec. IV, the physical control parameters that must be prescribed in any simulation run are the fluid density ρ and viscosity η, the interfacial width l, the applied shear rate $\dot{\gamma}$, and the system's aspect ratio Λ_x. (Recall that we have set $\Lambda_y=1$, $G=1$, and $\tau_0=1$.) We must also specify the number of numerical mesh points, N_x and N_y, and the numerical time step δ_t. We now discuss appropriate choices of these parameter values that will allow us to access the physical regimes of interest.

In the absence of an applied shear flow, $\dot{\gamma}=0.0$, our aim is to study coarsening of the isotropic domain morphology. See Fig. 3, for example. In each of these runs, we consider a square simulation box with $\Lambda_x=\Lambda_y=\Lambda=1$, in our units. In any given run, at any time t, our aim is to ensure a separation of the four length scales:

$$\delta \ll l \ll L(t) \ll \Lambda. \tag{38}$$

Here $\delta=1/N$ is the mesh size, prescribed by the reciprocal of the number $N=N_x=N_y$ of numerical mesh points in each spatial dimension. Recall that l is the width of the interface between domains, $L(t)$ is the growing domain size, and $\Lambda \equiv 1$ the system size. We thereby restrict ourselves to physical length scales l and $L(t)$ that lie between the mesh and system size. To make this window as large as possible, we take δ as small as possible, using as many grid points $N^2=1/\delta^2$ as is numerically feasible. The results presented below have $N=512$, checked for convergence to the limit $N\to\infty$ at fixed l against $N=1024$ (not shown). We set the interfacial width l to the minimum for which interfaces are still fully resolved by this grid, taking $l=0.00156$, checked for convergence to the limit $l/\Lambda\to 0$ against $l=0.0025$ and $l=0.005$ (not shown).

In each simulation run, this leaves a window of approximate size $0.05<L(t)<0.25$ in which the domain size $L(t)$ is much larger than the width l of the interface between domains and much smaller than the system size $\Lambda=1$. Accordingly, we are only able to study a small piece of the full curve $L(t)$ in each run. In different runs, therefore, we vary the viscosity η and density ρ to ensure that we cover all regimes of interest. As discussed in Refs. [46,47], we are then able to construct composite scaling curves $L(t)/L_{\mathrm{DV}}$ and $L(t)/L_{\mathrm{VI}}$, each spanning several decades of scaled length and time.

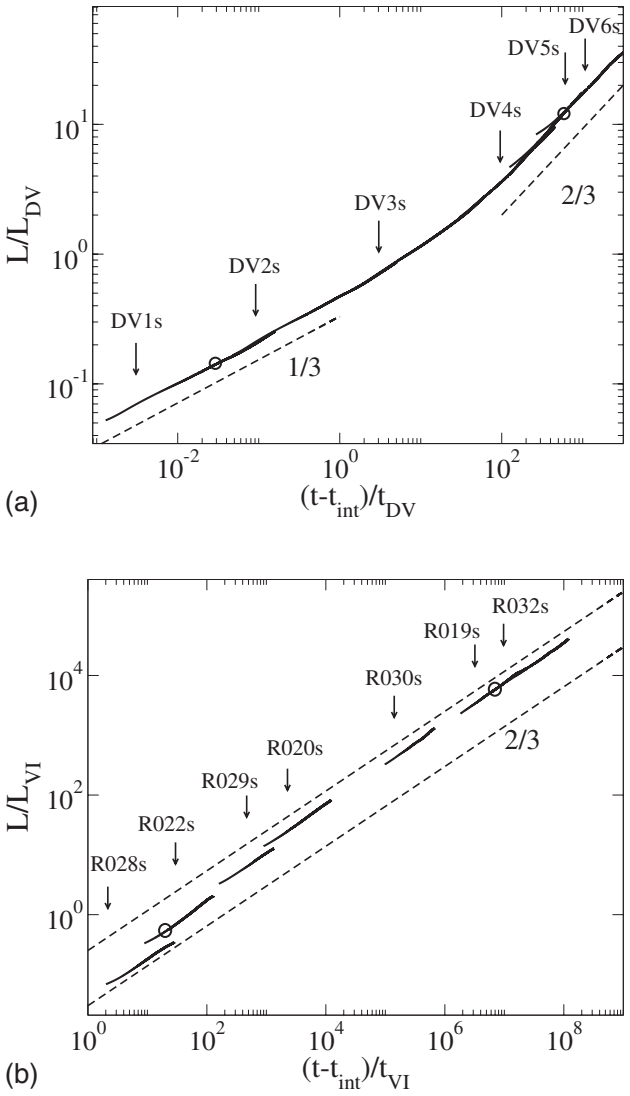

FIG. 2. (a) Scaled domain size versus scaled time for coarsening in zero shear in the diffusive and viscous hydrodynamic regimes. Segments from left to right correspond to runs DV1u–DV6u. The vertical arrows show the values of scaled reciprocal shear rate used in each corresponding run DV1s–DV6s. Circles show the times of the top two snapshots of Fig. 3 below. (b) Scaled domain size versus scaled time for coarsening in zero shear in the viscous and inertial hydrodynamic regimes. Segments from left to right correspond to runs R028u, R022u, R029u, R020u, R030u, R019u, and R032u. The vertical arrows show the values of scaled reciprocal shear rate used in each corresponding run R028s–R032s. Circles show the times of the bottom two snapshots of Fig. 3 below.

Below we present results for two different series of runs. In the first, R028u–R032u in Table I(a), we explore the viscous and inertial hydrodynamic regimes, and the crossover between them, by varying the crossover length scale L_{VI}. These are in fact the parameter values used previously by Kendon and co-workers in their lattice Boltzmann simulations [42], converted into our units.

In the second series of runs, DV1u–DV6u in Table I(b), we explore the diffusive and (again) viscous hydrodynamic regimes, and the crossover between them. Accordingly, we

TABLE I. Parameter values used in simulation runs.

Set	η	ρ	l	$\dot{\gamma}$	Λ_x	N_x	N_y	δ_t	L_{DV}	L_{VI}
(a) Zero applied shear. Viscous hydrodynamic to inertial hydrodynamic regime.										
R028u	0.111	136.0	0.00156	0.0	1.0	512	512	0.008	0.000519	0.0616
R022u	0.196	2510.0	0.00156	0.0	1.0	512	512	0.008	0.000690	0.0104
R029u	0.0467	893.0	0.00156	0.0	1.0	512	512	0.008	0.000337	0.00166
R020u	0.0785	16180.0	0.00156	0.0	1.0	512	512	0.008	0.000437	0.000259
R030u	0.0122	6250.0	0.00156	0.0	1.0	512	512	0.008	0.000172	0.0000162
R019u	0.00876	32814.0	0.00156	0.0	1.0	512	512	0.008	0.000146	0.00000159
R032u	0.00391	20067.0	0.00156	0.0	1.0	512	512	0.008	0.0000975	0.000000518
(b) Zero applied shear. Diffusive to viscous hydrodynamic regime.										
DV1u	1000.0	0.0	0.00156	0.0	1.0	512	512	0.016	0.0494	∞
DV2u	100.0	0.0	0.00156	0.0	1.0	512	512	0.016	0.0156	∞
DV3u	10.0	0.0	0.00156	0.0	1.0	512	512	0.016	0.00494	∞
DV4u	1.0	0.0	0.00156	0.0	1.0	512	512	0.016	0.00156	∞
DV5u	0.3	0.0	0.00156	0.0	1.0	512	512	0.016	0.000855	∞
DV6u	0.1	0.0	0.00156	0.0	1.0	512	512	0.016	0.000494	∞
(c) Applied shear, with inertia.										
R028s	0.111	136.0	0.00156	0.0765	2.0	1024	512	0.008	0.000519	0.0616
R028bs	0.444	8704.0	0.00156	0.0765	2.0	1024	512	0.008	0.00104	0.0154
R022s	0.196	2510.0	0.00156	0.0205	2.0	1024	512	0.008	0.000690	0.0104
R022bs	0.339	22590.0	0.00156	0.0355	2.0	1024	512	0.008	0.000908	0.00349
R029s	0.0467	893.0	0.00156	0.0341	2.0	1024	512	0.008	0.000337	0.00166
R029bs	0.0809	8037.0	0.00156	0.0591	2.0	1024	512	0.008	0.000444	0.000554
R020s	0.0785	16180.0	0.00156	0.0256	2.0	1024	512	0.008	0.000437	0.000259
R030s	0.0122	6250.0	0.00156	0.0410	2.0	1024	512	0.004	0.000172	0.0000162
R019s	0.00876	32814.0	0.00156	0.0251	2.0	1024	512	0.004	0.000146	0.00000159
R032s	0.00391	20067.0	0.00156	0.051	2.0	1024	512	0.004	0.0000975	0.000000518
(d) Applied shear, without inertia.										
DV1s	1000.0	0.0	0.00156	0.01	2.0	1024	512	0.016	0.0494	∞
DV2s	100.0	0.0	0.00156	0.01	2.0	1024	512	0.016	0.0156	∞
DV3s	10.0	0.0	0.00156	0.01	2.0	1024	512	0.016	0.00494	∞
DV4s	1.0	0.0	0.00156	0.01	2.0	1024	512	0.016	0.00156	∞
DV5s	0.3	0.0	0.00156	0.01	2.0	1024	512	0.016	0.000855	∞
DV6s	0.1	0.0	0.00156	0.03	2.0	1024	512	0.016	0.000494	∞

set $\rho=0$ such that L_{VI} is infinite and the inertial regime is never attained. Across the different runs we vary the predicted crossover length scale $L_{\mathrm{DV}}=l\sqrt{\eta}$ by sweeping the viscosity in the range $\eta=10^{-2}-10^{4}$. For the largest viscosity values, the system explores the diffusive regime. For the smallest values, the system passes into the viscous regime as soon as well defined domains have formed, without any identifiable regime of diffusive domain growth.

To study the effect of an applied shear flow, we consider the same sets of parameter values as in zero shear but now with nonzero values of $\dot{\gamma}$. In anticipation of the anisotropy that shear will induce, we also double the length of cell in the flow direction, along with N_x to maintain a constant density of mesh points. See Tables I(c) and I(d): as just discussed, the parameters of any sheared run (R032s, for example) are the same as those of the corresponding unsheared run (R032u), apart from the values of $\dot{\gamma}$, Λ_x, and N_x. The parameters of runs R028s, R022s, R029s, R020s, R030s, R019s, and R032s are those used in the lattice Boltzmann study of Ref. [38], converted into our units. The appearance of the new sets R028b, R022b, and R029b will be explained in Sec. VIII B below.

Assuming for the moment—in some cases incorrectly, as we shall show below—that any sheared system will attain a steady state with a typical domain size set by the reciprocal shear rate, our aim would then be to construct scaling plots $L(1/\dot{\gamma})$ analogous to those of $L(t)$ for the zero-shear coarsening regime in Fig. 2. To obtain as much information as in Fig. 2, however, we would need to run for very many values of the shear rate $\dot{\gamma}$ to produce corresponding near continuous

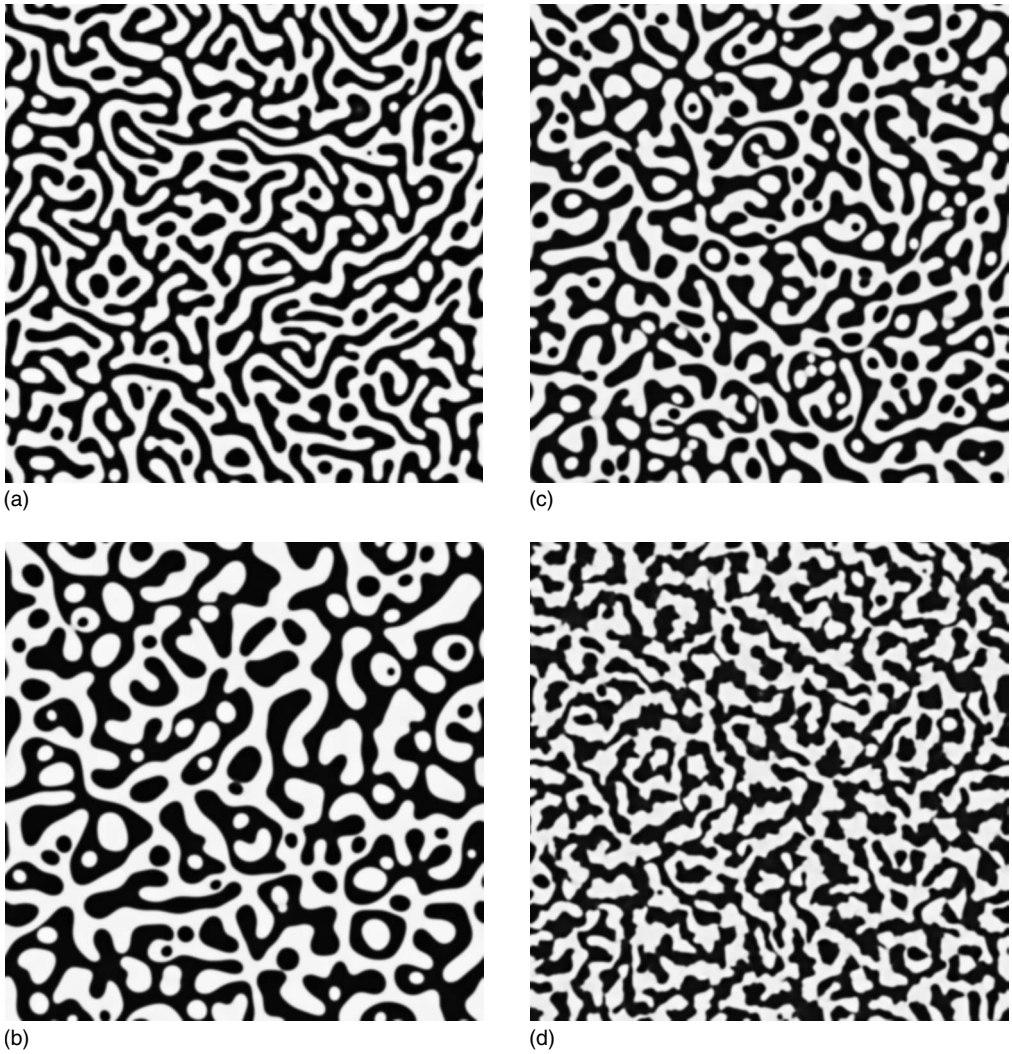

FIG. 3. Snapshots of domain morphology during coarsening in zero shear at the times shown by circles in Fig. 2. (a) Diffusive regime run DV1u at $t=1052$. (b) Viscous hydrodynamic regime run DV5u at $t=131$. (c) Viscous hydrodynamic regime run R022 at $t=78.9$. (d) Inertial hydrodynamic regime run R019 at $t=78.9$. Each subfigure shows the entire simulation domain, $\Lambda_x \times \Lambda_y = 1 \times 1$ in our units.

segments of L versus $1/\dot{\gamma}$. This is prohibitive within available computing resources. Accordingly, we ran for just one shear rate for each set of (other) parameter values, marking the scaled reciprocal shear rates recorded in Tables I(c) and I(d) with vertical arrows in Fig. 2.

VIII. NUMERICAL RESULTS

We now present the results of our numerical simulations. We start in Sec. VIII A with the case of coarsening in zero shear, before considering an applied shear flow with and without inertia in Secs. VIII B and VIII D, respectively. Section VIII C contains a linking discussion. Our aim in Secs. VIII A and VIII B is simply to reproduce behavior seen earlier in the literature by lattice Boltzmann techniques [38,41,42]. The purpose of this comparative part of our study is threefold: First, and foremost, to develop confidence in our own algorithm and the code via which it is implemented; second, to demonstrate the method used here, which is potentially simpler and faster than lattice Boltzmann, to be equally capable of capturing the physics of demixing, in 2D at least; and third, to provide an independent check of some recent results concerning nonequilibrium steady states under shear [38].

In each run, we take as an initial condition at each grid point a value of ϕ chosen at random from a flat probability distribution between −0.01 and +0.01. We checked for independence with respect to this initial condition (not shown) the statistical properties of the domain morphologies presented below. This independence holds as long as many domains are present, making the system self-averaging. Accordingly, for each set of parameters we give results below for a single simulation run only.

A. Zero shear

Following a temperature quench into the two phase regime, domains of each phase form. These progressively

coarsen in size through the action of surface tension, passing through growth regimes that are successively dominated by diffusive, viscous, and inertial dynamics. Within these regimes, dimensional analysis predicts a functional dependence of the characteristic domain size upon time of $L_D \propto t^{1/3}$, $L_V \propto t$, and $L_I \propto t^{2/3}$, respectively, as discussed in Sec. VI. Our aim in this section is to investigate this behaviour numerically, as done previously by lattice Boltzmann methods [41,42].

As noted in Sec. VII, only a small segment of the full coarsening curve $L(t)$ can be explored in any simulation run. Accordingly, in different runs we vary the viscosity η and density ρ. In this way we correspondingly vary the crossover length scales L_{DV} and L_{VI}. We then combine the data sets from the different runs into composite scaling curves of L/L_{DV} and L/L_{VI}, each spanning several decades in scaled length and time. We choose as our measure of L the one defined in Eq. (36) via the structure factor.

To explore the diffusive and viscous hydrodynamic regimes, and the crossover between them, we performed a single simulation run for each set of parameter values of Table I(b). The composite curve of L/L_{DV} is shown in Fig. 2(a). For each segment of the curve, three manipulations were performed. (i) The first $t=0-40$ time units were discarded to allow for transient dynamics during the initial process of domain formation. (ii) A time offset t_{int} was subtracted from the time t to allow for these nonuniversal dynamics during the initial transient. In each case this subtraction was performed by eye. The appropriate t_{int} was chosen as that which gives the most convincing straight line on a log-log plot, without any known power present to bias the eye during this process. (iii) The data set was cutoff at long times once the typical domain size approaches the system size. For this measure of the domain size, we used $L<0.02$ as a very conservative criterion ensuring this. The same manipulations were performed for runs in Table I(a), to be described below.

For small values of L/L_{DV}, in the diffusive regime, we recover the power $L_D \propto t^{1/3}$ predicted by dimensional analysis. This was confirmed previously by lattice Boltzmann simulations [41]. For large values of L/L_{DV}, in the viscous hydrodynamic regime, dimensional analysis predicts the growth law $L_V \propto t$. We instead find $L \propto t^{2/3}$ for each run. This anomalous scaling been observed previously, by lattice Boltzmann simulations. It is believed to stem from a breakdown of scale invariance in this regime in 2D, due to the formation of disconnected droplets [41], perhaps relating to the absence of the Rayleigh instability of tubes [48] in 2D. As a result of this breakdown, different measures of L depend differently on time (not shown here). In 3D (not studied here) scale invariance is recovered, along with the growth exponent of 1 [42].

To study the inertial hydrodynamic regime and (again) the viscous hydrodynamic regime, and the crossover between them, we use the parameter values of Table I(a). The composite curve of L/L_{VI} is shown in Fig. 2(b). For large values of L/L_{VI}, in the inertial regime, we clearly recover the predicted power $L_I \propto t^{2/3}$. This has been seen before, in three dimensions, by lattice Boltzmann simulations [42]. For small values of L/L_{VI}, in the viscous hydrodynamic regime, we again find the anomalous power $L \propto t^{2/3}$ for each run. This is consistent with the breakdown of scale invariance in 2D and its attendant departure from the predictions of dimensional analysis [41]. Because of this breakdown, segments R028, R022, R029, and R029 are not colinear: we do not have a single composite scaling curve in this regime. The fact that each segment follows a $t^{2/3}$ power, apparently the same as in the inertial regime, is a coincidence resulting from having chosen the particular measure of domain size given by Eq. (36). As already noted, the lack of scaling in this regime results in different power laws for different measures of the domain size [41]. Typical snapshots during domain coarsening are shown in Fig. 3.

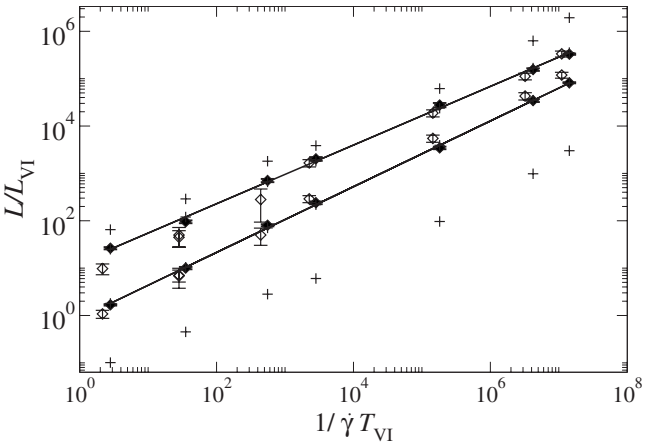

FIG. 4. Dimensionless scaling plot of lengths vs shear rate. Solid symbols: average of time series of Fig. 5 for $L_\parallel, L_\perp$ for strains $\dot{\gamma}t > 100$. Symbols from left to right correspond to R028bs, R022bs, R029bs, R020s, R030s, R019s, and R032s. Errors bars show the standard deviation. Solid lines: power law fits to the solid symbols, suggesting $L_\parallel \sim \dot{\gamma}^{-0.619}$ and $L_\perp \sim \dot{\gamma}^{-0.693}$. Upper set of crosses shows the scaled system size Λ_y/L_{VI}; lower set shows the scaled interfacial width l/L_{VI}. Open symbols: data from Ref. [38] for $L_\parallel, L_\perp$, reproduced here for comparison by kind permission of the authors of that study.

B. Under shear, with inertia

We now turn to phase separation in the presence of an applied shear flow. The main question of interest here is whether shear arrests coarsening and restores a nonequilibrium steady state with a finite domain size set by the reciprocal shear rate, independent of the system size, or whether coarsening persists indefinitely, up to the system size, even under shear.

Despite previous experimental [4–14], numerical [15–31], and theoretical [18–21,29,32–37] work, this question remained open until the recent simulation study of Stansell *et al.* in Ref. [38]. Using lattice Boltzmann techniques, they found nonequilibrium steady states of the type reproduced by our own simulations in Fig. 6. As expected under shear, the domain morphology is anisotropic. Accordingly, two length scales are needed to characterize it. The domain lengths L_x and L_y for the steady states were extracted in Ref. [38] via the curvature tensor of Eq. (37), and scaling plots of

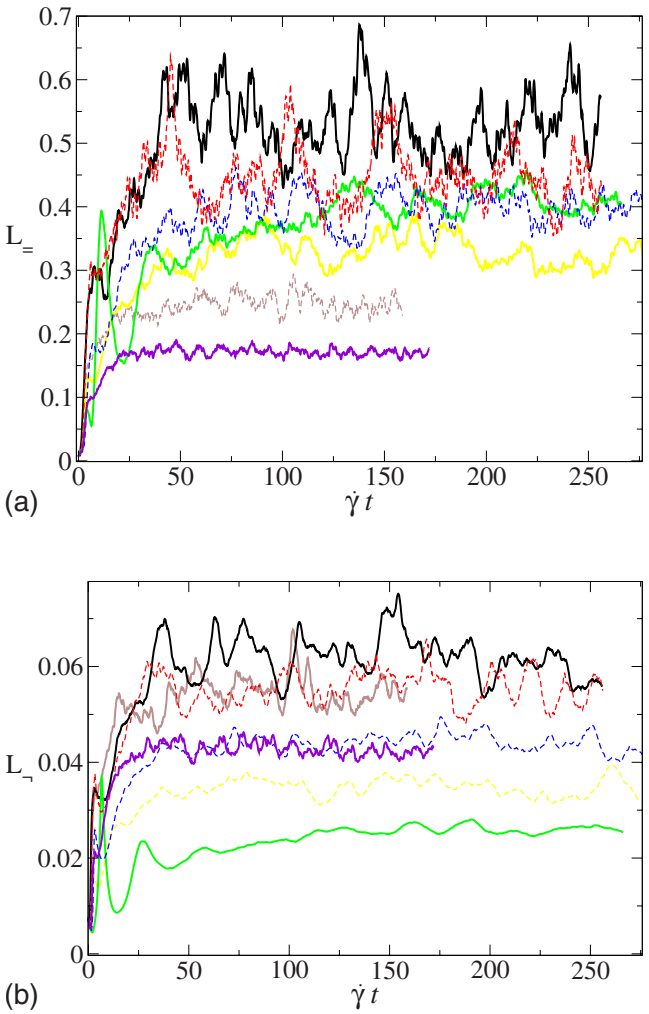

FIG. 5. (Color online) (a) Larger domain length vs strain $\dot{\gamma}t$. Data sets for decreasing values of long-term temporal average correspond to R020s, R030s, R028b, R029bs, R022bs, R019s, and R032s. (b) Smaller domain length vs strain. Data sets for decreasing values of long-term temporal average correspond to R020s, R030s, R019s, R029bs, R032s, R022bs, and R028b.

$L_{\{x,y\}}/L_{\mathrm{VI}}$ versus $1/\dot{\gamma}T_{\mathrm{VI}}$ were constructed. These suggested apparent scaling exponents $L_x \sim \dot{\gamma}^{-2/3}$ and $L_y \sim \dot{\gamma}^{-3/4}$, sustained over six decades. The same scalings $L_{\parallel} \sim \dot{\gamma}^{-2/3}$ and $L_{\perp} \sim \dot{\gamma}^{-3/4}$ were suggested for the major and minor principal lengths of the domains. Slightly different scalings, discussed below, were obtained by the same group in a more recent 3D study [39].

In this section we aim to show that our simulations, which are in 2D throughout, reproduce the earlier results to good approximation. We will thereby gain confidence in our technique, before proceeding to the novel contribution of this work in Sec. VIII D below. Accordingly, we perform a single simulation run for each set of parameter values used in Ref. [38], converted into our units. See R028, R022, R029, R020, R030, R019, and R032 in Table I(c). The small discrepancy in the imposed values of $1/\dot{\gamma}T_{\mathrm{VI}}$, evident in Fig. 4, stems from a slightly different definition adopted for the interfacial width, realized by this author only at a late stage of the present study.

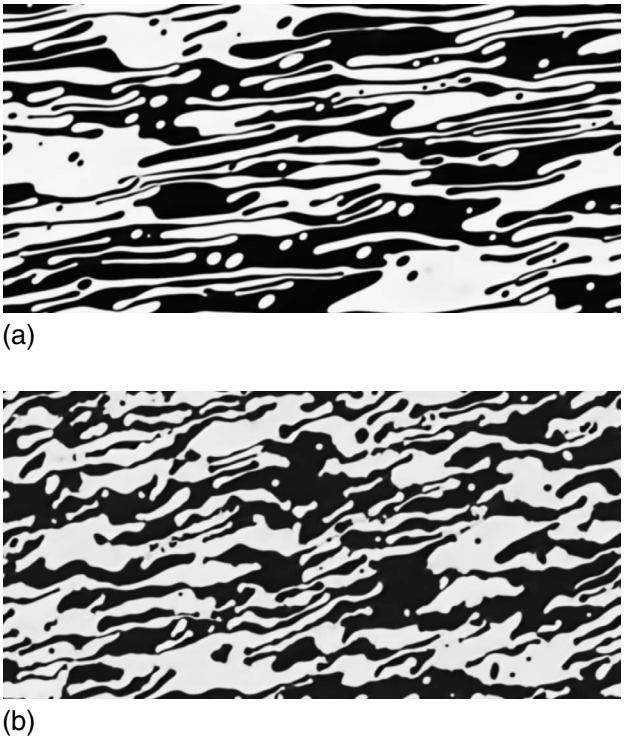

FIG. 6. Snapshots of the steady-state order parameter for R022b at strain $\dot{\gamma}t=112$ (a) and R032 at strain $\dot{\gamma}t=161$ (b).

A typical run took 1–2 weeks of wall-clock time on a Linux box, given exclusive use of a single 3.4-GHz Intel Xeon CPU with 2-Mb cache and 400-MHz DDR2 memory. Approximately 70% of the run time appears to be used switching back and forth between real and reciprocal space at each time step.

In each run, we monitored as a function of time the characteristic domain sizes $L_{\parallel}$ and $L_{\perp}$ extracted from the tensor of Eq. (37). For each of R020, R030, R019, and R032 we found $L_{\parallel}$ and $L_{\perp}$ to saturate at long times, showing temporal fluctuations about constant mean values (Fig. 5). For the remainder of this section we focus only on these statistically steady states, neglecting the first $\dot{\gamma}t=100$ strain units of each run. (This cutoff was chosen by a simple visual inspection of Fig. 5.) In each case, finite-size effects appear under control, as seen in the order parameter snapshots of Fig. 6. The mean values of the time series are shown on the scaling plot of L/L_{VI} versus $1/\dot{\gamma}T_{\mathrm{VI}}$ in Fig. 4, with error bars showing the standard deviation. A snapshot of the order parameter for run R032 is shown in Fig. 6(b).

For runs R028, R022, and R029, in contrast, we found the domains to wrap completely around the system in the flow direction, eventually comprising trivial horizontal stripes connected at the edges of the cell by the periodic boundary conditions. We believe this to be due to the horizontal system size Λ_x being dangerously close to the expected values of $L_{\parallel}$ for these runs, leading eventually to nucleation of these stripes.

To eliminate this effect, we performed new runs R028b, R022b, and R029b at the same prescribed values of $1/\dot{\gamma}T_{\mathrm{VI}}$ as for R028, R022, and R029, but now for larger values of

the scaled system size $\Lambda_x/L_{\mathrm{VI}}$. This was achieved by adjusting L_{VI} at fixed $\Lambda_x, \dot{\gamma}T_{\mathrm{VI}}$. Effectively, the left three sets of crosses in Fig. 4 have been slightly shifted upward with respect to those in Ref. [38]. These new runs produced nonequilibrium steady states, as seen in the time series of Fig. 5. The long-term time averages of these series are shown in the scaling plot of Fig. 4. A snapshot of the order parameter for run R022b is shown in Fig. 6(a).

Of course we cannot rule out eventual nucleation of system-wrapped stripes at times exceeding those accessed numerically. The same comment applies to runs R028, R029, and R022 of Ref. [38]. Conversely, the system-wrapped stripes seen in the corresponding runs in the recent 3D lattice Boltzmann study [39] might well be eliminated by adjusting the scaled system size as done here.

Power law fits to our data in the scaling plot of Fig. 4 suggest exponents $L_{\parallel} \sim \dot{\gamma}^{-0.619\pm0.01}$ and $L_{\perp} \sim \dot{\gamma}^{-0.693\pm0.007}$. The quoted uncertainties are the standard deviations given by the automated regression package and do not include systematic errors in the simulations. In contrast Ref. [38] found exponents for $L_{\parallel}$ and $L_{\perp}$ of -0.678 ± 0.039 and -0.756 ± 0.03, by fitting to the open symbols that are reproduced by kind permission in Fig. 4 for comparison with our data. It also quoted exponents for L_x and L_y of -0.678 ± 0.042 and -0.759 ± 0.029. The more recent 3D study [39] by the same group found exponents for $L_{\parallel}$ and $L_{\perp}$ of -0.64 ± 0.06 and -0.67 ± 0.03, with -0.53 ± 0.04 in the third dimension. Within their $O(10\%)$ margins of error, these agree with the exponents for $L_{\parallel}$ and $L_{\perp}$ found in the 2D study of the present work.

C. Discussion

In this section, we will discuss in more detail the shape of the scaling plot of L/L_{VI} versus $1/\dot{\gamma}T_{\mathrm{VI}}$ in Fig. 4. In doing so, we will motivate the further numerical study of Sec. VIII D below.

Translated into equivalent scaled times t/T_{VI}, the range of scaled shear rates $1/\dot{\gamma}T_{\mathrm{VI}}$ explored in Fig. 4 would span the viscous and inertial hydrodynamic regimes in the coarsening plot of Fig. 2(b). One possibility for the shape of the scaling curve L/L_{VI} versus $1/\dot{\gamma}T_{\mathrm{VI}}$ under shear is that it should be the same as that of the corresponding coarsening plot of L/L_{VI} versus t/T_{VI} in zero shear, given the simple substitution $t=\dot{\gamma}^{-1}$. In view of this, it is instructive to compare Fig. 4 with Fig. 2(b) in some detail.

In the coarsening case [Fig. 2(b)], two distinct regimes are apparent. The inertial hydrodynamic regime, on the right-hand side, shows the $t^{2/3}$ exponent predicted by dimensional analysis. Each segment neatly lines up with the next, consistent with dynamical scaling. In contrast, in the viscous hydrodynamic regime on the left-hand side the segments do not align. Furthermore, each departs from the predicted t^1 power. As noted above, these anomalous features stem from nonscaling effects that arise in 2D. In 3D these are suppressed and the predicted t^1 power law is recovered. The counterpart of Fig. 2(b) for 3D systems thus comprises a clean t^1 in the viscous regime on the left-hand side and $t^{2/3}$ in the inertial regime on the right-hand side, with a rather slow crossover in between. See Fig. 9 of Ref. [42]. An applied shear flow is also anticipated to suppress these nonscaling effects. Accordingly, the 2D results of Fig. 4 are expected capture the basic physics and, indeed, compare favorably with the recent 3D sheared study of Ref. [42].

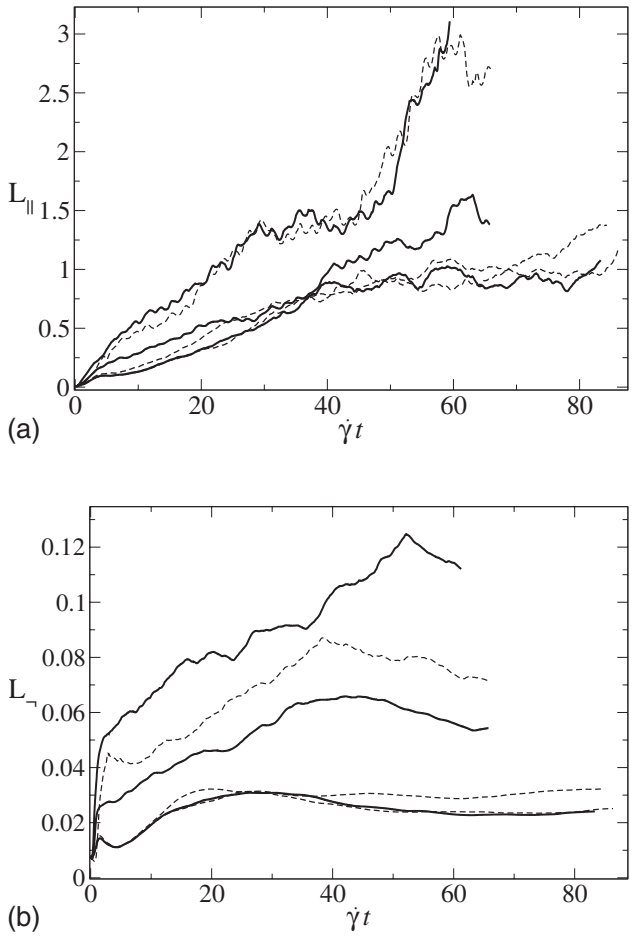

FIG. 7. (a) Larger domain length $L_{\parallel}$ vs strain $\dot{\gamma}t$. (b) smaller domain length $L_{\perp}$ vs strain $\dot{\gamma}t$. In each case, decreasing values of L at fixed $\dot{\gamma}t=15$ correspond to runs DV5s, DV6s, DV4s, DV3s, DV2s, and DV1s.

With these remarks in mind, it is now clear that we should in fact compare Fig. 4 for sheared systems with Fig. 9 of Ref. [42] for coarsening systems. As noted above, one might naively expect the two plots to have the same shape, up to the substitution $t=\dot{\gamma}^{-1}$.

Instead, two differences are clearly apparent. First, Fig. 4 has two characteristic lengths, in contrast to the single length that characterizes unsheared systems in Fig. 2(b). With hindsight this is obvious: the domain morphology is anisotropic in sheared systems and so characterized by two lengths.

The second, and more subtle, difference is that sheared systems apparently lack a distinction between viscous and inertial regimes, with a single power law spanning all six decades in Fig. 4. A possible explanation for this is that the range of scaled shear rates in Fig. 4 actually occupies a window of extremely slow crossover between a true viscous regime at smaller $1/\dot{\gamma}T_{\mathrm{VI}}$ and a true inertial regime at larger $1/\dot{\gamma}T_{\mathrm{VI}}$, reminiscent of the slow crossover seen in the coars-

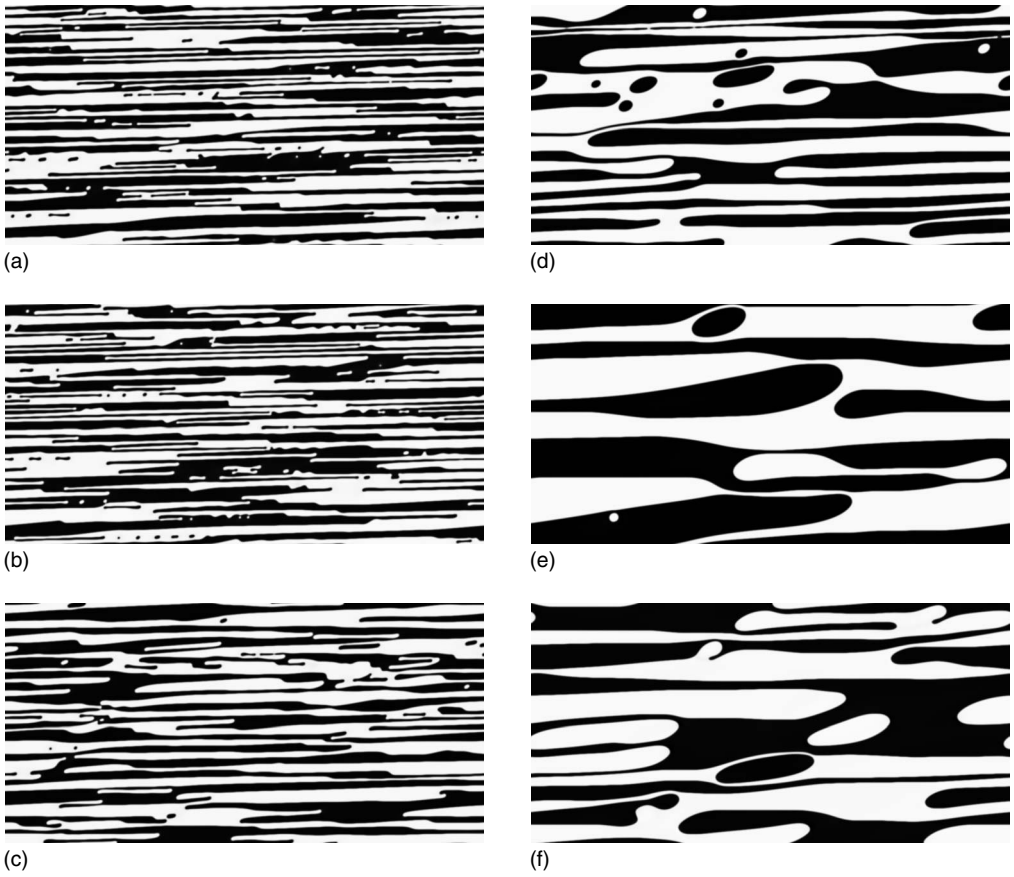

FIG. 8. Snapshot domain morphologies after many strain units $S=\dot{\gamma}t$ for reciprocal shear rates that, as equivalent times $\dot{\gamma}^{-1}$, would be shown by the arrows in Fig. 2(a). (a) DV1s, $\dot{\gamma}t=78.9$; (b) DV2s, $\dot{\gamma}t=78.9$; (c) DV3s, $\dot{\gamma}t=78.9$; (d) DV4s, $\dot{\gamma}t=63.2$; (e) DV5s, $\dot{\gamma}t=55.3$; (f) DV6s, $\dot{\gamma}t=47.4$. All these runs have zero inertia, $\rho=0$.

ening plot in Ref. [42]. Another is that the value of $1/\dot{\gamma}T_{\mathrm{VI}}$ at which the crossover occurs in the sheared case is much smaller than the corresponding crossover value of t/T_{VI} in the unsheared case, which is formally $O(1)$ but in practice lies around 10^4. The results in Fig. 4 would then all lie in the inertial regime, to the right of this crossover.

To test these ideas, in the next section we perform simulations at strictly zero Reynolds number, $\rho=0$. We thereby take the limit $\dot{\gamma}T_{\mathrm{VI}}\to\infty$ at the outset and perform simulations for several finite values of $1/\dot{\gamma}T_{\mathrm{DV}}$. When converted into equivalent scaled times t/T_{DV} these span the diffusive and viscous hydrodynamic regimes, as shown by the vertical arrows in Fig. 2(a). By analogy with the fact that the 3D counterpart of the viscous regime of Fig. 2(a) would be expected in the limit $t/T_{\mathrm{DV}}\to\infty$ to match into that of the viscous regime in Fig. 9 of Ref. [42] in the limit $t/T_{\mathrm{VI}}\to 0$, we might then expect to access, for large $1/\dot{\gamma}T_{\mathrm{DV}}\to\infty$, the scalings that $L_{\parallel}$ and $L_{\perp}$ would attain in the limit $1/\dot{\gamma}T_{\mathrm{VI}}\to 0$ at the extreme left of an enlarged Fig. 4.

Instead, however, we will find no evidence for nonequilibrium steady states in inertialess systems. In contrast, coarsening appears to persist indefinitely, up to the system size, despite the applied shear flow. Given the existence of nonequilibrium steady states for values of $1/\dot{\gamma}T_{\mathrm{VI}}$ at the left-hand edge of Fig. 4, where the effects of inertia are nonzero but likely to be small, this suggests that inertia plays the role of a singular perturbation in this problem. Indeed, we will argue in Sec. IX below that the single scaling seen for each of $L_{\parallel}$ and $L_{\perp}$ across Fig. 4 results from a *mixed* visco-inertial regime across the entire plot. The crisis of infinite aspect ratio $L_{\parallel}/L_{\perp}\to\infty$ in the limit $1/\dot{\gamma}/T_{\mathrm{VI}}\to 0$, suggested by the data in Fig. 4, is consistent with our suggestion that inertia plays a singular role.

D. Under shear, without inertia

Motivated by the discussion of the previous section we now consider phase separation under shear in inertialess systems, setting $\rho=0$. As just discussed, by studying the limit $t/T_{\mathrm{DV}}\to\infty$ we might then, *a priori*, have expected to gain some insight into the far left-hand side of an enlarged Fig. 4, $1/\dot{\gamma}T_{\mathrm{VI}}\to 0$. Accordingly, we perform a single simulation run for each of the parameter sets DV1s–DV6s in Table I(d). The values of the scaled reciprocal shear rates $1/\dot{\gamma}T_{\mathrm{DV}}$ are marked as corresponding scaled times t/T_{DV} on the coarsening plot of Fig. 2(a), where they are seen to span both the diffusive and viscous hydrodynamic regimes.

In each run we monitored the characteristic domain sizes $L_{\parallel}$ and $L_{\perp}$ as a function of time. As can be seen in Fig. 7, in each case the larger length $L_{\parallel}$ grows without bound until it attains the system size $O(1)$. Correspondingly, a snapshot of the order parameter after many strain units reveals system-

wrapped domains, with pronounced finite-size effects (see Fig. 8). The snapshots for DV1s–DV3s strongly resemble those reported in Ref. [31] for model *B*, which lacks hydrodynamics. This is consistent with the fact that these runs occupy the diffusive regime when marked as equivalent scaled times in Fig. 2(b).

Beyond the parameter sets of Table I(d), we furthermore performed runs for shear rates $\dot{\gamma}=0.1,0.03,0.01,0.003$ at each value of the viscosity $\eta=1000.0,100.0,10.0,1.0,0.3,0.1$, thereby covering a complete rectangle in $(\eta,\dot{\gamma})$ space, in contrast to the single slice taken by DV1s–DV6s. (For historical reasons these runs had a slightly larger value $l=0.0025$ for the interfacial width, but we do not expect this to make a qualitative difference.) We found no evidence in any run for a nonequilibrium steady state, unlimited by finite-size effects.

These results clearly suggest that the limit $1/\dot{\gamma}T_{\mathrm{DV}}\to\infty$, which is approximated by runs DV5s and DV6s, does not match the limit $1/\dot{\gamma}T_{\mathrm{VI}}\to 0$, which is approximated by runs R028b and R022b. In the next section, we propose that this is because the limit $1/\dot{\gamma}T_{\mathrm{DV}}\to\infty$ corresponds to a pure viscous regime in which no steady state exists, while the limit $1/\dot{\gamma}T_{\mathrm{VI}}\to 0$ corresponds to a mixed visco-inertial regime in which a steady state does exist.

IX. ABSENCE OF NONEQUILIBRIUM STEADY STATES IN INERTIALESS SYSTEMS

We now present an analytical argument in support of the above numerical observation: that nonequilibrium steady states are not attained in inertialess systems. As we shall find, a closely related argument supports the existence of a single power law for each of $L_{\parallel}$ and $L_{\perp}$ across the whole of Fig. 4, as seen first in Ref. [38]. Recall that, *a priori*, we might have expected this plot to comprise separate viscous and inertial regimes.

As a preliminary step, we recall the case of domain coarsening in an unsheared system. As discussed above, as time proceeds the system passes through regimes that are successively dominated by diffusive, viscous, and inertial dynamics. In each regime, the system is aware of the surface tension σ, the time t, and either the mobility M (diffusive regime), the viscosity η (viscous regime), or the density ρ (inertial regime). In each case, there exists only one possible combination of these relevant parameters that has the dimensions of a length. Thus we have the following predicted growth laws for the characteristic domain size:

$$L_{\mathrm{D}}=(M\sigma t)^{1/3},\quad L_{\mathrm{V}}=\frac{\sigma t}{\eta},\quad L_{\mathrm{I}}=\left(\frac{\sigma t^2}{\rho}\right)^{1/3}. \tag{39}$$

Consider next a nonequilibrium steady state under shear. Neglecting fluctuations, the time t is now irrelevant. In its place, however, we gain the reciprocal shear rate as a relevant parameter. If "pure" diffusive, viscous, and inertial regimes were still to exist, then we could again only construct a *single* length scale to characterize each:

$$L_{\mathrm{Ds}}=(M\sigma\dot{\gamma}^{-1})^{1/3},\quad L_{\mathrm{Vs}}=\frac{\sigma\dot{\gamma}^{-1}}{\eta},\quad L_{\mathrm{Is}}=\left(\frac{\sigma\dot{\gamma}^{-2}}{\rho}\right)^{1/3}, \tag{40}$$

by direct comparison with (39).

In contrast, however, our numerical results clearly show the domain morphology to be anisotropic, as expected in a sheared system. It is therefore characterized by *two* lengths, which (according to Fig. 4) scale differently with the applied shear rate. A steady state under shear therefore cannot exist in a "pure" diffusive, viscous, or inertial regime, because in each there are insufficient parameters out of which to construct the two length scales needed to characterize it.

How can we retain enough parameters, out of the candidates σ, $\dot{\gamma}$, M, ρ, η, and t, to construct the two length scales needed to characterize an anisotropic domain morphology under shear? Assuming that σ and $\dot{\gamma}$ are always relevant, two options are as follows.

(i) If the system is to exist in a *pure diffusive, viscous, or inertial regime*, with knowledge of just one of M, η, or ρ (as well as σ and $\dot{\gamma}$), it must retain dependence on time t. Therefore, it must *fail to attain a steady state*.

Assuming power laws, a purely diffusive regime would then have

$$L_{\mathrm{Ds}}=(M\sigma t)^{1/3}(\dot{\gamma}t)^{a}, \tag{41}$$

in which a assumes two different values, which would be prescribed by more detailed physics than is contained in the present argument. Likewise, a purely viscous regime would have

$$L_{\mathrm{Vs}}=\frac{\sigma t}{\eta}(\dot{\gamma}t)^{b}, \tag{42}$$

again with two different values for b.

(ii) If the system is to attain a *steady state*, thereby losing knowledge of the time t, it must retain dependence upon at least two of M, η, and ρ. For example, a shear-induced steady state that is free of diffusion on the length scale of domains (no M) must exist in a *mixed viscous-inertial regime* with knowledge of both viscosity η and density ρ:

$$L_{\mathrm{VIs}}=(\rho^{-c-1}\eta^{c}\sigma\dot{\gamma}^{-2-c})^{1/2c+3}, \tag{43}$$

with two different values for c.

We propose that both of these cases are seen in our numerical simulations. When inertia is present, for finite values of ρ (however small), the system exists in a mixed visco-inertial steady state, as discussed in option (ii). This is consistent with the observation of a single power law scaling for each of $L_{\parallel}$ and $L_{\perp}$ across all six decades in the plot of L/L_{VI} versus $1/\dot{\gamma}T_{\mathrm{VI}}$ in Fig. 4 and in Ref. [38]. In contrast, when inertia is strictly absent ($\rho=0$, infinite $\dot{\gamma}T_{\mathrm{VI}}$), the system exists in a pure diffusive or viscous regime and never attains a steady state, as in option (i).

To summarize, we suggest that the limit $1/\dot{\gamma}T_{\mathrm{DV}} \to \infty$ corresponds to a pure viscous regime with no steady state, while the limit $1/\dot{\gamma}T_{\mathrm{VI}} \to 0$ corresponds to a mixed visco-inertial steady state. Thus we propose finally that inertia provides the role of a singular perturbation in this problem.

X. SUMMARY AND OUTLOOK

We have studied numerically phase separation in binary fluids with full hydrodynamics in two dimensions, considering both (1) unsheared and (2) sheared systems, both (a) with and (b) without inertia. Of these, cases (1a), (1b), and (2a) have been studied by previous authors using lattice Boltzmann (LB) methods [28,38,41,42]. In this paper, we have introduced an alternative simulation technique that uses finite-differencing and spectral methods. We have also used a convenient transformation to render trivial the implementation of Lees-Edwards sheared periodic boundary conditions [40].

In unsheared systems, phase separation occurs via a process of domain coarsening. Our simulation method successfully recovers results obtained previously by LB for this process, both with and without inertia [(1a) and (1b) above]. In particular, it finds the familiar power law $L_{\mathrm{D}} \sim t^{1/3}$ characterizing the growth of the typical domain size in the diffusive regime [41]. It also recovers $L_{\mathrm{I}} \sim t^{2/3}$ in the inertial hydrodynamic regime [42]. In the viscous hydrodynamic regime it finds the anomalous power $L \sim t^{2/3}$, compared to the predicted one of $L_{\mathrm{v}} \sim t^{1}$. As noted by previous authors, this is due to subtle nonscaling effects that arise in 2D from the formation of disconnected droplets, also seen in LB studies [41]. Such effects are eliminated in 3D [42] and also seem suppressed under shear [28,38].

We have also successfully reproduced the observations of existing LB studies for sheared systems that have nonzero inertia [case (2a) above] [38]. Here, an applied shear flow arrests domain coarsening and restores a nonequilibrium steady state with domains of a finite-size set by the inverse shear rate. The domain morphology is anisotropic, characterized by two length scales $L_{\parallel}$ and $L_{\perp}$. Scaling exponents $L_{\parallel} \sim \dot{\gamma}^{-0.619}$ and $L_{\perp} \sim \dot{\gamma}^{-0.693}$ found here agree with those of the LB method, to within margins of error. An outstanding puzzle, however, is why these 2D exponents agree better with the exponents $L_{\parallel} \sim \dot{\gamma}^{-0.64}$ and $L_{\perp} \sim \dot{\gamma}^{-0.67}$ of the 3D LB study [39] than those of the 2D LB study [38], $L_{\parallel} \sim \dot{\gamma}^{-0.678}$ and $L_{\perp} \sim \dot{\gamma}^{-0.756}$. To investigate this, it would be interesting to study the role of systematic errors in our simulations, to consider the possible eventual nucleation of system wrapping stripes in the 2D LB study of Ref. [38] for the smaller values of $1/\dot{\gamma}T_{\mathrm{VI}}$, and to extend the present finite-differencing work to 3D.

Our successful recovery of these important existing results in regimes [(1a), (1b), (2a)] provides some confidence in our simulation method. Beyond thereby having demonstrated this method to be capable of capturing the physics of demixing, the other main contribution of this paper has been a novel study of phase separation in sheared systems that are strictly inertialess [case 2b]. Here we found no evidence of nonequilibrium steady states free of pronounced finite size effects. Instead coarsening appears to persist indefinitely until the typical domain size attains the system size, as in zero shear.

To support this observation, we have suggested by means of a simple analytical argument that sheared inertialess systems adopt either a pure diffusive or pure viscous regime, in each of which there are insufficient parameters out of which to construct the two length scales needed to characterize an anisotropic domain morphology in steady state. By extending this argument slightly, we have also suggested that sheared systems with any amount of inertia, however small, exist in a mixed visco-inertial steady state. This provides a possible explanation for the observation of a single scaling with shear rate for each of $L_{\parallel}$ and $L_{\perp}$ across all six decades in Fig. 4 and in the corresponding plot of Ref. [38].

If this suggestion is correct, it remains unclear why the viscous and inertial regimes should mix to yield a steady state, while the diffusive and viscous regimes apparently remain separate, precluding nonequilibrium steady states in truly inertialess systems. A possible explanation lies in the more severe nonlinearity (in $\boldsymbol{v}$) of the inertial terms in the equation of motion.

In future work, we aim to investigate whether the absence of nonequilibrium steady states in inertialess systems persists in 3D. In extending our method to 3D, several challenges are to be faced. Of these, the main ones appear to be contained in the basic Navier-Stokes equations of incompressible fluid flow and are not complicated significantly by any additional order parameters [49]: ϕ in this model. However, relatively standard methods do exist for finite-differencing the incompressible Navier-Stokes equations in 3D, as discussed in Ref. [50]. At each time step these involve updating the vorticity via a slightly modified equation of motion, $\partial_t \omega = \cdots$, and then updating the velocity field either in the velocity-vorticity formulation (as effectively done here in 2D via the intermediate of the stream function) or in the vector potential-vorticity formulation. In neither case does the pressure field need to be calculated directly. An outstanding issue before any such algorithm could be run efficiently concerns its scaling with system size and its corresponding ease of parallelization. The same question is also relevant in 2D, and a direct comparison of our algorithm with that of Ref. [38] would clearly be interesting. In the longer term, the outcome of such studies might help determine whether finite differencing can emerge as a useful tool in such problems, alongside the already tested and reliable LB methods.

Other open questions concern the role of initial conditions in sheared systems. All the simulations reported here consider a temperature quench performed in the presence of a shear flow. Future work should consider an already demixed system, with either a flat interface or a minimal-surface droplet, subsequently subject to a sudden shear startup. We also aim to address demixing in complex macromolecular fluids, focusing on the role of viscoelasticity.

ACKNOWLEDGMENTS

The author thanks Professor Alan Bray, Professor Mike Cates, and Professor Peter Sollich for helpful discussions and

feedback and the UK's EPSRC GR/S29560/02 for funding.

APPENDIX A: TRANSFORMATION TO THE COSHEARED FRAME

Here we give details of the transformation to the cosheared frame [40]. As discussed in Sec. V above, this is performed in order to render trivial the numerical implementation of sheared periodic boundary conditions. As a first step, we separate the velocity field into a constant affine contribution $\dot{\gamma} y \hat{\boldsymbol{x}}$ and a fluctuating part $\tilde{\boldsymbol{v}}$:

$$\boldsymbol{v}(\boldsymbol{x},t) = \dot{\gamma} y \hat{\boldsymbol{x}} + \tilde{\boldsymbol{v}}(\boldsymbol{x},t). \tag{A1}$$

Noting that $\dot{\gamma} y \hat{\boldsymbol{x}}$ automatically satisfies the incompressibility condition, we define the fluctuating parts of the stream function and vorticity via

$$\tilde{\boldsymbol{v}} = \boldsymbol{\nabla} \wedge \tilde{\psi} \hat{\boldsymbol{z}} \tag{A2}$$

and

$$\tilde{\omega} = -\nabla^2 \tilde{\psi}. \tag{A3}$$

Our equation set then comprises Eqs. (A2) and (A3) together with

$$\rho(\partial_t \tilde{\omega} + \tilde{\boldsymbol{v}} \cdot \boldsymbol{\nabla} \tilde{\omega}) + \rho \dot{\gamma} y \partial_x \tilde{\omega} = \eta \nabla^2 \tilde{\omega} - [\boldsymbol{\nabla} \wedge \phi \boldsymbol{\nabla} \mu] \cdot \hat{\boldsymbol{z}}, \tag{A4}$$

from Eq. (3),

$$\partial_t \phi + \tilde{\boldsymbol{v}} \cdot \boldsymbol{\nabla} \phi + \dot{\gamma} y \partial_x \phi = l^2 \nabla^2 \mu, \tag{A5}$$

from Eq. (7), and

$$\mu = \phi(\phi^2 - 1) - l^2 \nabla^2 \phi, \tag{A6}$$

from Eq. (8), unchanged.

We then make a transformation to the cosheared frame:

$$(x,y,t) \to (x' = x - \dot{\gamma} t y, y' = y, t' = t). \tag{A7}$$

The various partial derivatives then become

$$(\partial_x, \partial_y, \partial_t) = (\partial_{x'}, -\dot{\gamma} t \partial_{x'} + \partial_{y'}, -\dot{\gamma} y \partial_{x'} + \partial_{t'}). \tag{A8}$$

Accordingly, we define the cosheared 2D gradient operator

$$\boldsymbol{\nabla}_c = \hat{\boldsymbol{x}} \partial_{x'} + \hat{\boldsymbol{y}}(-\dot{\gamma} t \partial_{x'} + \partial_{y'}). \tag{A9}$$

Finally, for any function a we write

$$a(x,y,t) = A(x',y',t'). \tag{A10}$$

Throughout we continue to work with velocity components $\tilde{v}_x, \tilde{v}_y$ and not $\tilde{v}_{x'}, \tilde{v}_{y'}$.

Inserting Eq. (A2) into the $\tilde{\boldsymbol{v}} \cdot \boldsymbol{\nabla}$ terms on the LHS of Eqs. (A4) and (A5), and performing the transformation from (A7)–(A10) on Eqs. (A3)–(A6), we get the equation set

$$\tilde{\Omega} = -\nabla_c^2 \tilde{\Psi}, \tag{A11}$$

together with

$$\rho \partial_{t'} \tilde{\Omega} + \rho(\partial_{y'} \tilde{\Psi} \partial_{x'} \tilde{\Omega} - \partial_{x'} \tilde{\Psi} \partial_{y'} \tilde{\Omega}) = \eta \nabla_c^2 \tilde{\Omega} - [\partial_{x'} \Phi \partial_{y'} M - \partial_{y'} \Phi \partial_{x'} M], \tag{A12}$$

$$\partial_{t'} \Phi + (\partial_{y'} \tilde{\Psi} \partial_{x'} \Phi - \partial_{x'} \tilde{\Psi} \partial_{y'} \Phi) = l^2 \nabla_c^2 M, \tag{A13}$$

and

$$M = \Phi(\Phi^2 - 1) - l^2 \nabla_c^2 \Phi. \tag{A14}$$

In these M represents uppercase μ, not mobility. *A priori*, the bracketed expressions in Eqs. (A12) and (A13) contain terms in the applied shear rate $\dot{\gamma}$. However, in each set of brackets these are equal and opposite, and so cancel. For clarity we finally drop the tildes and dashes, and revert from uppercase to lowercase. The final governing equations are then as summarized in Sec. V above.

APPENDIX B: NUMERICAL METHOD

Here we discuss the numerical algorithm used to study the dynamical evolution of $\phi(\boldsymbol{x},t)$, $\omega(\boldsymbol{x},t)$, and $\psi(\boldsymbol{x},t)$, as specified by Eqs. (21)–(24) and (26). Our basic strategy is to step along a grid of time values $t^n = n\Delta t$ for $n = 1,2,3,\ldots$. Discretization with respect to time of any quantity f is denoted $f(t^n) = f^n$, or sometimes by $f|^n$. At each time step, we update $\phi^n, \psi^n, \omega^n \to \phi^{n+1}, \psi^{n+1}, \omega^{n+1}$ in three separate stages. First, we update the compositional order parameter $\phi^n \to \phi^{n+1}$ according to Eqs. (23) and (24) with fixed, old values of the stream function ψ^n. We then update $\omega^n \to \omega^{n+1}$ using Eq. (22) at fixed ϕ^{n+1} and ψ^n. Finally we update the stream function $\psi^n \to \psi^{n+1}$ using Eq. (21) at fixed ω^{n+1}.

(i) The update $\phi^n \to \phi^{n+1}$ using Eqs. (23) and (24) is performed in two successive partial updates. In the first we implement the advective term in Eq. (23) to give $\phi^n \to \phi^{n+1/2}$. In the second we implement the diffusive term to give $\phi^{n+1/2} \to \phi^{n+1}$. The advective term is handled using an explicit Euler algorithm [51]. Temporarily setting aside the issue of spatial discretization, this can be written

$$\phi^{n+1/2}(x,y) = \phi^n - \Delta t(\partial_y \psi^n \partial_x \phi^n - \partial_x \psi^n \partial_y \phi^n). \tag{B1}$$

This is then spatially discretized on a rectangular grid of $(\Lambda_x N/\Lambda_y) \times N$ mesh points in real space $(x-y)$, with constant mesh intervals $\delta_x = \delta_y = \Lambda_y/N$. Using indices $i = 1,\ldots,\Lambda_x N/\Lambda_y$ and $j = 1,\ldots,N$, we denote any discretized function $f(x_i,y_j) = f_{ij}$, or sometimes $f|_{ij}$. Periodic boundary conditions are imposed by setting $f_{i(-1)} = f_{i(N-1)}$, $f_{i0} = f_{iN}$, $f_{i(N+1)} = f_{i1}$, and $f_{i(N+2)} = f_{i2}$, and similarly in the x direction. The derivatives of ψ in Eq. (B1) are discretized as follows:

$$\partial_x \psi|_{ij}^n = \frac{1}{2\delta_x}[\psi_{(i+1)j} - \psi_{(i-1)j}], \tag{B2}$$

with

$$\partial_y \psi|_{ij}^n = \frac{1}{2\delta_y}\left\{\left(1 - \frac{s}{2}\right)(\psi_{i(j+1)} - \psi_{i(j-1)}) + \frac{s}{2}(\psi_{(i-2)(j+1)} - \psi_{(i+2)(j-1)})\right\} \quad \text{if } s \geqslant 0, \tag{B3}$$

and

$$\partial_y \psi|_{ij}^n = \frac{1}{2\delta_y}\left\{\left(1+\frac{s}{2}\right)(\psi_{i(j+1)} - \psi_{i(j-1)}) - \frac{s}{2}(\psi_{(i+2)(j+1)} - \psi_{(i-2)(j-1)})\right\} \quad \text{if } s<0. \quad \text{(B4)}$$

The derivatives of ϕ in Eq. (B1) are discretized in the same way.

It then remains to implement the diffusive part of Eq. (23):

$$\partial_t \phi = -l^2\nabla_c^2\phi - l^4\nabla_c^4\phi + l^2\nabla_c^2 f, \quad \text{(B5)}$$

with $f=\phi^3$. After calculating f on our rectangular grid in real space, this equation is handled in reciprocal space by taking fast Fourier transforms $x\to q_x$ and $y\to q_y$ using a standard NAG routine [52]. The transformation in each dimension generates a real and an imaginary part, so for each mode $\boldsymbol{q}=(q_x,q_y)$ we need to consider a vector of the (transposed) form $\phi^T=(\phi_{\rm rr},\phi_{\rm ir},\phi_{\rm ri},\phi_{\rm ii})$ where subscript "r" denotes real part and "i" imaginary. The respective transforms $\boldsymbol{D}_2$ and $\boldsymbol{D}_4$ of the operators $l^2\nabla_c^2$ and $l^4\nabla_c^4$ can easily be found analytically:

$$\boldsymbol{D}_2 = l^2\begin{pmatrix} D & 0 & 0 & -\Delta \\ 0 & D & \Delta & 0 \\ 0 & \Delta & D & 0 \\ -\Delta & 0 & 0 & D \end{pmatrix},$$

$$\boldsymbol{D}_4 = l^4\begin{pmatrix} D^2+\Delta^2 & 0 & 0 & -2D\Delta \\ 0 & D^2+\Delta^2 & 2D\Delta & 0 \\ 0 & 2D\Delta & D^2+\Delta^2 & 0 \\ -2D\Delta & 0 & 0 & D^2+\Delta^2 \end{pmatrix}, \quad \text{(B6)}$$

in which

$$D = -(aq_x^2+q_y^2), \quad \Delta = bq_xq_y \quad \text{with } a=1+[s(t)]^2, \quad b=2s(t). \quad \text{(B7)}$$

For each $\boldsymbol{q}$ mode, we then have

$$\partial_t\phi = -\boldsymbol{D}_2\cdot\phi - \boldsymbol{D}_4\cdot\phi + \boldsymbol{D}_2\cdot\boldsymbol{f}. \quad \text{(B8)}$$

To evolve this in time, we use an explicit Euler algorithm for the first and third terms and a semi-implicit Crank-Nicolson algorithm for the second term. Thus we have

$$\phi^{n+1} - \phi^{n+1/2} = -\tilde{\boldsymbol{D}}_2\cdot\phi^{n+1/2} - \frac{1}{2}\tilde{\boldsymbol{D}}_4\cdot(\phi^{n+1}+\phi^{n+1/2}) + \tilde{\boldsymbol{D}}_2\cdot\boldsymbol{f}^n, \quad \text{(B9)}$$

in which $\tilde{\boldsymbol{D}}_m=\delta_t\boldsymbol{D}_m$ for $m=2,4$. Rearranging gives finally

$$\phi^{n+1} = \phi^{n+1/2} + \left(\boldsymbol{\delta}+\frac{1}{2}\tilde{\boldsymbol{D}}_4\right)^{-1}\cdot(-\tilde{\boldsymbol{D}}_2\cdot\phi^{n+1/2} - \tilde{\boldsymbol{D}}_4\cdot\phi^{n+1/2} + \tilde{\boldsymbol{D}}_2\cdot\boldsymbol{f}^n). \quad \text{(B10)}$$

(ii) We now update $\omega^n\to\omega^{n+1}$ using Eq. (22) at fixed ϕ^{n+1}, ψ^n. The advective term on the LHS is updated in the same way as its counterpart in the ϕ equation above. To avoid inefficient multiple switching between real and Fourier space, this is in fact done at the same time as the corresponding update of ϕ in 1. above. (This reordering leaves the algorithm exactly unchanged.) We then update the RHS of Eq. (22). Divided across by ρ, this reads

$$\partial_t\omega = \nu\nabla_c^2\omega + g, \quad \text{(B11)}$$

in which $\nu=\eta/\rho$ and

$$g = -\frac{1}{\rho}[\partial_x\phi\partial_y\mu - \partial_y\phi\partial_x\mu]. \quad \text{(B12)}$$

As a first step, we calculate $g(x,y)$ using the newly updated ϕ^{n+1} from 1. To do so, we first calculate

$$\mu = \phi(\phi^2-1) - l^2(1+[s(t)]^2)\partial_x^2\phi - l^2\partial_y^2\phi + 2l^2s\partial_x\partial_y\phi. \quad \text{(B13)}$$

At each grid point i, j, we spatially discretize the derivatives in this expression according to

$$\partial_x^2\phi|_{ij} = \frac{1}{(\delta_x)^2}[\phi_{(i+1)j} - 2\phi_{ij} + \phi_{(i-1)j}], \quad \text{(B14)}$$

similarly for $\partial_y^2\phi$, and

$$\partial_x\partial_y\phi|_{ij} = \frac{1}{4\delta_x\delta_y}[\phi_{(i+1)(j+1)} - \phi_{(i+1)(j-1)} - \phi_{(i-1)(j+1)} + \phi_{(i-1)(j-1)}]. \quad \text{(B15)}$$

The first-order derivatives of ϕ and μ with respect to x and y in Eq. (B12) are then discretized as in Eq. (B2).

Having calculated $g(x,y)$ in real space, we then Fourier transform Eq. (B11) to get

$$\partial_t\boldsymbol{\omega} = \boldsymbol{C}\cdot\boldsymbol{\omega} + \boldsymbol{g}, \quad \text{(B16)}$$

in which we have used the same vector and matrix notation as in (i) above, with $\boldsymbol{C}=\nu\boldsymbol{D}_2/l^2$. To evolve this in time, we use a semi-implicit Crank-Nicolson algorithm for the first term on the RHS to get

$$\boldsymbol{\omega}^{n+1} - \boldsymbol{\omega}^n = \frac{1}{2}\tilde{\boldsymbol{C}}\cdot(\boldsymbol{\omega}^n+\boldsymbol{\omega}^{n+1}) + \tilde{\boldsymbol{g}}^{n+1}, \quad \text{(B17)}$$

with $\tilde{\boldsymbol{C}}=\delta_t\boldsymbol{C}$ and $\tilde{\boldsymbol{g}}=\delta_t\boldsymbol{g}$. The superscript $n+1$ on the last term (B17) serves to remind us that g was calculated using the new ϕ^{n+1} from part (i). Rearranging, we get finally

$$\boldsymbol{\omega}^{n+1} = \boldsymbol{\omega}^n + \left(\boldsymbol{\delta} - \frac{1}{2}\tilde{\boldsymbol{C}}\right)^{-1}\cdot(\tilde{\boldsymbol{C}}\cdot\boldsymbol{\omega}^n + \tilde{\boldsymbol{g}}^{n+1}). \quad \text{(B18)}$$

(iii) We finally update the stream function $\psi^n\to\psi^{n+1}$ using Eq. (21) at fixed ω^{n+1}. For each $\boldsymbol{q}$ mode, we have

$$\psi^{n+1} = -\boldsymbol{E}\cdot\boldsymbol{\omega}^{n+1}$$

in which

$$\boldsymbol{E} = \frac{1}{D^2 - \Delta^2} \begin{pmatrix} D & 0 & 0 & \Delta \\ 0 & D & -\Delta & 0 \\ 0 & -\Delta & D & 0 \\ \Delta & 0 & 0 & D \end{pmatrix}. \tag{B19}$$

Finally, we transform all functions back to real space and return to step (i) to start the next time step.

Algorithm at zero Reynolds number

The algorithm discussed so far is suited to nonzero values of the fluid density ρ. At zero Reynolds number, with $\rho=0$, Eqs. (21) and (22) of our basic equation set combine to give the simpler equation

$$0 = -\eta \nabla_c^4 \psi - [\partial_x \phi \partial_y \mu - \partial_y \phi \partial_x \mu], \tag{B20}$$

and we need no longer consider the vorticity field ω. Equations (23) and (24) remain unchanged. Correspondingly, step (i) of our algorithm is also unchanged. Steps (ii) and (iii) now combine to give

$$\psi^{n+1} = \boldsymbol{E} \cdot \boldsymbol{g}^{n+1}. \tag{B21}$$

As above, we calculate g in real space then take a Fourier transform. In Fourier space,

$$\boldsymbol{E} = \frac{1}{(D^2 + \Delta^2)^2 - (2D\Delta)^2} \times \begin{pmatrix} D^2 + \Delta^2 & 0 & 0 & 2D\Delta \\ 0 & D^2 + \Delta^2 & -2D\Delta & 0 \\ 0 & -2D\Delta & D^2 + \Delta^2 & 0 \\ 2D\Delta & 0 & 0 & D^2 + \Delta^2 \end{pmatrix}. \tag{B22}$$

After calculating ψ, we revert to real space to start the next time step.

[1] P. C. Hohenberg and B. I. Halperin, Rev. Mod. Phys. **49**, 435 (1977).
[2] A. J. Bray, Adv. Phys. **43**, 357 (1994).
[3] M. E. Cates, V. M. Kendon, P. Bladon, and J. C. Desplat, Faraday Discuss. **112**, 1 (1999).
[4] T. Hashimoto, T. Takebe, and S. Suehiro, J. Chem. Phys. **88**, 5874 (1988).
[5] Y. Takahashi, N. Kurashima, I. Noda, and M. Doi, J. Rheol. **38**, 699 (1994).
[6] C. K. Chan, F. Perrot, and D. Beysens, Phys. Rev. A **43**, 1826 (1991).
[7] A. H. Krall, J. V. Sengers, and K. Hamano, Phys. Rev. Lett. **69**, 1963 (1992).
[8] T. Hashimoto, K. Matsuzaka, E. Moses, and A. Onuki, Phys. Rev. Lett. **74**, 126 (1995).
[9] D. Beysens, M. Gbadamassi, and B. Moncef-Bouanz, Phys. Rev. A **28**, 2491 (1983).
[10] C. K. Chan, F. Perrot, and D. Beysens, Phys. Rev. Lett. **61**, 412 (1988).
[11] K. Matsuzaka, T. Koga, and T. Hashimoto, Phys. Rev. Lett. **80**, 5441 (1998).
[12] E. K. Hobbie, S. H. Kim, and C. C. Han, Phys. Rev. E **54**, R5909 (1996).
[13] F. Qiu, J. D. Ding, and Y. L. Yang, Phys. Rev. E **58**, R1230 (1998).
[14] J. Lauger, C. Laubner, and W. Gronski, Phys. Rev. Lett. **75**, 3576 (1995).
[15] Z. Y. Shou and A. Chakrabarti, Phys. Rev. E **61**, R2200 (2000).
[16] Z. L. Zhang, H. D. Zhang, and Y. L. Yang, J. Chem. Phys. **113**, 8348 (2000).
[17] R. Yamamoto and X. C. Zeng, Phys. Rev. E **59**, 3223 (1999).
[18] F. Corberi, G. Gonnella, and A. Lamura, Phys. Rev. Lett. **81**, 3852 (1998).
[19] F. Corberi, G. Gonnella, and A. Lamura, Phys. Rev. Lett. **83**, 4057 (1999).
[20] F. Corberi, G. Gonnella, and A. Lamura, Phys. Rev. E **61**, 6621 (2000).
[21] F. Corberi, G. Gonnella, and A. Lamura, Phys. Rev. E **62**, 8064 (2000).
[22] D. H. Rothman, Phys. Rev. Lett. **65**, 3305 (1990).
[23] D. H. Rothman, Europhys. Lett. **14**, 337 (1991).
[24] C. K. Chan and L. Lin, Europhys. Lett. **11**, 13 (1990).
[25] F. Qiu, H. D. Zhang, and Y. L. Yang, J. Chem. Phys. **108**, 9529 (1998).
[26] P. Padilla and S. Toxvaerd, J. Chem. Phys. **106**, 2342 (1997).
[27] T. Ohta, H. Nozaki, and M. Doi, J. Chem. Phys. **93**, 2664 (1990).
[28] A. J. Wagner and J. M. Yeomans, Phys. Rev. E **59**, 4366 (1999).
[29] A. Lamura and G. Gonnella, Physica A **294**, 295 (2001).
[30] A. Lamura, G. Gonnella, and F. Corberi, Eur. Phys. J. B **24**, 251 (2001).
[31] L. Berthier, Phys. Rev. E **63**, 051503 (2001).
[32] A. Onuki, J. Phys.: Condens. Matter **9**, 6119 (1997).
[33] A. J. Bray, Philos. Trans. R. Soc. London, Ser. A **361**, 781 (2003).
[34] A. Cavagna, A. J. Bray, and R. D. M. Travasso, Phys. Rev. E **62**, 4702 (2000).
[35] A. J. Bray and A. Cavagna, J. Phys. A **33**, L305 (2000).
[36] A. Onuki, J. Phys.: Condens. Matter **9**, 6119 (1997).
[37] M. Doi and T. Ohta, J. Chem. Phys. **95**, 1242 (1991).
[38] P. Stansell, K. Stratford, J.-C. Desplat, R. Adhikari, and M. E. Cates, Phys. Rev. Lett. **96**, 085701 (2006).
[39] K. Stratford, J.-C. Desplat, P. Stansell, and M. E. Cates, Phys. Rev. E **76**, 030501(R) (2007).
[40] A. Onuki, J. Phys. Soc. Jpn. **66**, 1836 (1997).
[41] A. J. Wagner and J. M. Yeomans, Phys. Rev. Lett. **80**, 1429 (1998).
[42] V. M. Kendon, M. E. Cates, I. Pagonabarraga, J. C. Desplat, and P. Bladon, J. Fluid Mech. **440**, 147 (2001).
[43] M. R. Swift, E. Orlandini, W. R. Osborn, and J. M. Yeomans,

Phys. Rev. E **54**, 5041 (1996).
[44] E. D. Siggia, Phys. Rev. A **20**, 595 (1979).
[45] H. Furukawa, Adv. Phys. **34**, 703 (1985).
[46] V. M. Kendon, J. C. Desplat, P. Bladon, and M. E. Cates, Phys. Rev. Lett. **83**, 576 (1999).
[47] I. Pagonabarraga, A. J. Wagner, and M. E. Cates, J. Stat. Phys. **107**, 39 (2002).
[48] J. M. Yeomans, Annu. Rev. Comput. Phys. **7**, 61 (2000).
[49] D. Marenduzzo, E. Orlandini, M. E. Cates, and J. M. Yeomans, Phys. Rev. E **76**, 031921 (2007).
[50] C. Pozrikidis, *Introduction to Theoretical and Computation Fluid Dynamics* (Oxford University Press, New York, 1997).
[51] W. H. Press, S. A. Teukolsky, W. T. Vetterling, and B. P. Flannery, *Numerical Recipes in C*, 2nd ed. (Cambridge University Press, Cambridge, England, 1992).
[52] Numerical Algorithms Group Ltd., Wilkinson House, Jordan Hill Road, Oxford, OX2 8DR, UK.